Quantum dynamics of hydrogen interacting with single-walled carbon nanotubes
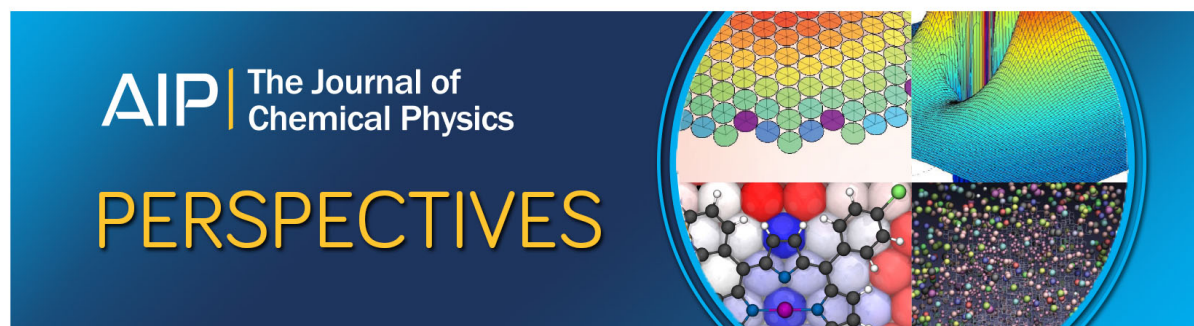
Jason L. McAfee, and Bill Poirier

Quantum dynamics of hydrogen interacting with single-walled carbon nanotubes

Jason L. McAfee[1] and Bill Poirier[1,2,a]
[1]*Department of Chemistry and Biochemistry, Texas Tech University, Lubbock, Texas 79409-1061, USA*
[2]*Department of Physics, Texas Tech University, Lubbock, Texas 79409-1061, USA*

We perform spin-polarized density functional theory calculations for a hydrogen atom interacting exohedrally with a (5,5) single-walled carbon nanotube (SWNT). We also perform full three-dimensional (3D) quantum dynamics calculations of the H atom bound rovibrational states. We initially focus on the four sites of highest symmetry, along which we compute potential energy surface (PES) values at 33 separate, nonuniformly spaced radial values. These 132 geometries are sufficient to define the primary potential interaction regions. We find a weak physisorptive region between 2.5 and 3.5 Å from the SWNT wall, with a maximum well depth of 51 meV, relative to the desorption limit. We also find a chemisorptive region, extending from about 1.0 out to 1.5 Å from the SWNT wall. The maximum well depth of 0.755 eV occurs at 1.15 Å from the SWNT wall, nearly directly above a carbon atom. A small barrier of 54 meV lies between these two binding regions. There are also two types of transition states that lie between adjacent chemisorption wells. In addition to the high-symmetry sites, a detailed and accurate characterization of the PES requires density functional theory calculations along a large number of interstitial sites—18 in all. Using these 18×33 geometries, and exploiting the full D_{10h} symmetry of the system, we fit a global analytical PES, using a Fourier basis in the cylindrical coordinates, with radially dependent expansion coefficients (rms error 3.8 meV). We then perform a mixed spectral basis/phase-space optimized discrete variable representation calculation of all bound rovibrational H atom eigenfunctions and energy levels. We also discuss ramifications for the possible use of SWNTs as hydrogen storage devices. © *2009 American Institute of Physics*. [DOI: 10.1063/1.3068411]

I. INTRODUCTION

A major hurdle to the development of technologies that utilize hydrogen is the lack of systems that can store and retrieve sufficient hydrogen for vehicular use in a safe, efficient, and compact manner. Toward this end, the U.S. Department of Energy (DoE) has set a goal for the development of storage technologies that are capable of storing 6% by weight hydrogen by 2010 and 9% by 2015.[1] Over the past decade, there have been thousands of publications on the subject of hydrogen storage using single-walled carbon nanotubes (SWNTs). The first experimental report of hydrogen storage by SWNTs (Ref. 2) shows a 5–10 wt % hydrogen storage capacity. However, in these early reports of high storage capacities—and many since[2–5]—there is some controversy,[5–9] owing to the fact that the experimental samples are far from pure, and it is not always clear exactly where and how the hydrogen is being stored—much less the mechanisms responsible.

Moreover, percent weight storage is hardly the only issue that one must contend with, when designing viable hydrogen storage materials. High volumetric and gravimetric storage capacities are equally important, as are other factors such as favorable enthalpies of hydrogen uptake/release, rapid reversible kinetics at ambient temperatures (T) and pressures (p), long cycle lifetimes, and of course, economic

viability.[1] The ideal storage material will facilitate fast and efficient removal of hydrogen as well as rapid and economical recharging at the hydrogen "gas pump." A great deal of effort, both experimental and theoretical, has been expended to elucidate the issues raised above, and a much clearer picture is now emerging than what could be discerned ten years ago. Nevertheless, much still remains obscure, such as a mechanistic level understanding, the precise role and nature of possible catalysts, etc., which may prove to be extremely important. Indeed, the DoE has recently concluded that achieving all of the above goals *cannot be accomplished through incremental progress*, but will require fundamental new research, aimed at promoting understanding of the basic physical and chemical processes related to the interaction of hydrogen with solid-state compounds.

Such is the current state of affairs, particularly in the field of carbon-based hydrogen storage materials. There is now a general consensus, for instance, that pure carbon nanostructures, in their pristine form, will *not* satisfy the target DoE goals[10]—at least not via the simplest direct adsorption mechanism—for reasons that will be discussed below. Nevertheless, carbon-based materials are increasingly seen as serious contenders for viable hydrogen storage media[1]—a "paradox" whose resolution requires the introduction of more complicated adsorption pathways such as the spillover mechanism, which are only poorly understood at present. Thus, whereas much progress has indeed been made, there

a)Electronic mail: bill.poirier@ttu.edu.

are still many fundamental questions that remain unanswered—or at best, contested.

In the theoretical arena, where density functional theory (DFT) has been the primary computational tool, this ambiguity can be attributed in part to the bewildering variety of DFT "flavors"—i.e., local density approximation versus generalized gradient approximation (GGA), the functional form used to compute the exchange-correlation energy, the explicit inclusion of spin, etc., as well as the general inability of DFT to provide error bars. Even more fundamentally, however, almost all previous DFT studies—even for the simplest case of the SWNT-H atom system—have artificially restricted the set of geometries so as to preclude certain mechanisms that might play an important role. The first challenge of this paper, therefore, is to construct an accurate, global potential energy surface (PES) that incorporates all possible (exohedral) H-atom geometries, and for which the *ab initio* values are converged as systematically as is possible for a DFT approach. This shall facilitate explicit consideration of all relevant reaction pathways, including those that have not previously been considered.

Constructing a global PES, however, is only the first step toward understanding the interaction between hydrogen and carbon nanotube (or other) storage materials; in our view, a thorough and unambiguous characterization also requires a *quantum dynamical* treatment—hydrogen being, after all, the most quantum of all atoms. The second major goal of this paper is therefore to perform accurate quantum dynamics calculations for all of the rovibrational bound states of the SWNT-H system. Perhaps remarkably, despite reams of literature, no previous full-dimensional [for the H-atom degrees of freedom (DOFs)] quantum dynamical studies appear to have been performed for this type of system—although a reduced-dimensional quantum dynamical study of endohedral confinement was recently published.[11] Endohedrally bound hydrogen in SWNTs is certainly also interesting, especially *vis-a-vis* quantum confinement or "seiving," as well as catalysis. In the hydrogen storage context, it may also play a role, *vis-a-vis* the spillover mechanism. However, the current work focuses only on the case of exohedral hydrogen adsorption.

Before delving into the details of the above calculations, we first find it prudent to provide a detailed overview of some of the previous findings, in as much as they relate to the present work. Regarding percent weight storages for pristine SWNTs—and notwithstanding a certain amount of remaining controversy—recent experimental[12] and theoretical[13] studies indicate that less than 1% hydrogen can be stored via direct adsorption at room temperature (T) and standard pressure (p), which is far less than the DoE target value. The above authors[13] concluded that the binding energy for the chemisorption mechanism is too high, and that of the physisorption mechanism (for H or H_2) too low, to achieve the desired storage characteristics at ambient T and p. According to the Langmuir isotherm model, the maximum delivery of hydrogen,[14] assuming $p=30$ bars for adsorption and $p=1.5$ bars for desorption, at ambient temperature

($T=298$ K), requires an adsorption enthalpy of 156 meV, i.e., intermediate in value between pure chemi- and physisorptions.

Although a general qualitative experimental[15–18] and theoretical[13,19–26] consensus has been reached in the above regard, it should be noted that stark quantitative disagreements are still found in the literature, *vis-a-vis* predicted SWNT-H binding energies. More specifically, the computed binding energy of atomic hydrogen to a (5,5) SWNT (the particular SWNT considered in this paper) varies from 0.4 up to 2.87 eV, depending on DFT flavor, degree of hydrogenation, substrate relaxation, etc. Note also that *none* of the above predictions incorporates zero-point energy (ZPE) even approximately—although ZPE will clearly be substantial, particularly (in a relative sense) for physisorption. An accurate calculation of the ZPE for the SWNT-H system requires a quantum dynamical treatment, and will thus be provided here for the first time.

Although pristine SWNTs fail to achieve DoE standards for hydrogen storage via a direct adsorption mechanism, at least two promising avenues still remain for the use of SWNTs in hydrogen storage. The first is modification of the SWNT substrate via the introduction of dopants or defects, which has already been shown to substantially enhance the adsorptive storage capacity of hydrogen by SWNTs.[4,27–29] This is due primarily to modifications in the electronic structure that are fairly well understood qualitatively—although quantitative agreement, e.g., of binding energies, has not yet been achieved and will in any case also require accurate quantum dynamical treatment.

The second avenue is the so-called spillover mechanism,[30–34] indicated schematically in Fig. 1. This mechanism utilizes a catalyst that dissociates the molecular H_2 bond and allows the resultant H atoms to migrate onto the SWNT. Once chemisorbed onto the SWNT wall, the H atoms must somehow migrate or diffuse along the wall away from the catalyst to make room for new H atoms to be adsorbed. The entire spillover process—molecular dissociation, atomic chemisorption, and migration—must be largely reversible, and indeed, experimental data suggest that it is.[30,31,35] However, the precise mechanism(s) involved remain largely a mystery. Note that one key dynamical property is the rate of H atom migration along the SWNT wall, which could easily turn out to be the bottleneck for the entire spillover process. An accurate elucidation of this mechanism—and quantitative prediction of the associated migration rates—will thus turn out to be an important by-product of our quantum dynamical calculation. Indeed, this analysis will lead to a partial explanation of reversibility, which could not have been predicted, even qualitatively, from the PES alone. Note also that for the spillover mechanism, the large chemisorption binding energies are actually desirable, in that the competing desorption pathway becomes highly energetically unfavorable at ambient T.

The goal of this paper is to completely characterize—comprehensibly and unambiguously—the fundamental interactions between an H atom and a pristine (5,5) SWNT. Although the SWNT C atom DOFs are held fixed at their equilibrium values, the three H atom DOFs are allowed to
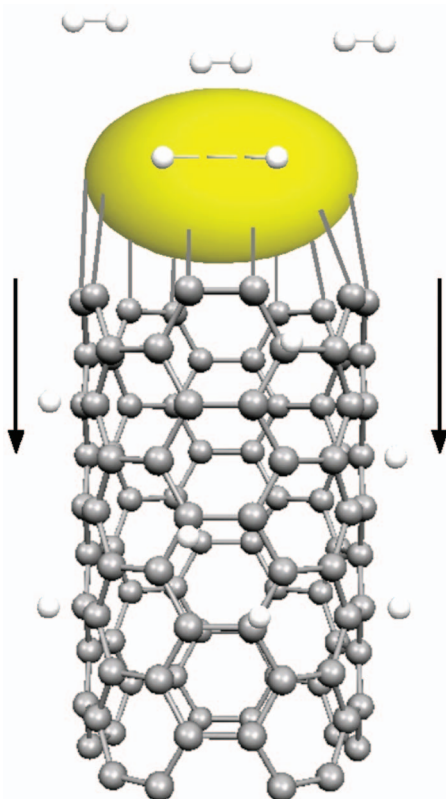
FIG. 1. (Color) Schematic of spillover mechanism for hydrogen on (5,5) SWNT. Free H_2 molecules are catalytically dissociated to form H atoms at the catalyst, indicated by the large oval attached to the top of the SWNT. The H atoms then chemisorb to the SWNT and migrate along the SWNT exterior.

vary arbitrarily—thus leading via accurately converged DFT calculations to a global three-dimensional (3D) PES for the SWNT-H interaction. This PES is then used to perform full-dimensional exact quantum dynamics calculations using a combination of phase-space optimized[36–39] discrete variable representation[40,41] (PSO-DVR) and symmetry-adapted basis set methods. Eigenfunctions and energy levels are computed for all bound rovibrational states, and from these are extracted ZPEs and migration rates for each irreducible representation (irrep) of the D_{10h} symmetry group. The latter are directly relevant for the migration portion of the spillover mechanism discussed above (the catalysis step is not considered here). The ZPE and characterization of chemisorptive versus physisorptive states are clearly relevant for understanding the desorption dynamics. These results may have an indirect bearing on hydrogen storage, in as much as similar techniques may be applied to SWNTs with defects or dopants—although such calculations are not actually performed here, but are reserved for future publications.

The remainder of this paper is organized as follows. Section II describes our use of DFT to generate an analytic PES and our implementation of basis set/PSO-DVR methods for performing the exact quantum dynamics calculations. Section III discusses the results of the DFT calculations, the PES fitting, parameters, and functional form, the energy levels and eigenfunctions as computed from the exact quantum dynamics calculation, ZPEs, state-specific migration rates, and ramifications for the use of SWNTs as hydrogen storage me-
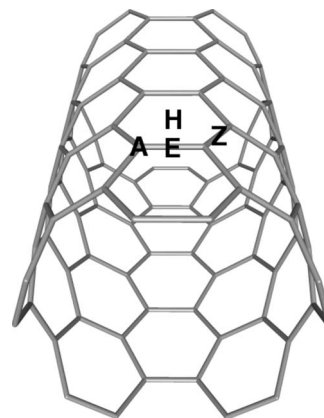

FIG. 2. Five unit cells of a (5,5) SWNT, showing the four sites of highest symmetry. The gray lines represent carbon-carbon bonds. The center of a hexagon is designated as the "*H*-site." The carbon atoms themselves constitute the "*A*-sites." The bridge site of an equatorial carbon-carbon bond is call an "*E*-site," whereas that of a zigzag bond along the SWNT axis is the "*Z*-site."

dia via the spillover mechanism—especially *vis-a-vis* reversibility. Concluding remarks, including a discussion of other application areas in which the ideas introduced here may prove useful, are provided in Sec. IV.

II. METHODOLOGY

A. Geometry, symmetry, and coordinates

We chose to study the (5,5) SWNT because of its curvature-induced strain and other features, and the fact that it is a standard benchmark for SWNT studies. The relatively small number of atoms in the unit cell, 20, also makes the (5,5) SWNT comparatively easy to study from the perspective of computational (CPU) cost. Figure 2 shows five unit cells, i.e., 100 carbon atoms, along with our naming convention for the four cylindrical sites (i.e., radial directions) of highest symmetry.

The unit cell of the (5,5) SWNT belongs to the point group D_{5d}. The infinite-length SWNT is built by translating the unit cell axially in the z direction by the distance z_0, the height of the unit cell. The infinite-length SWNT does not belong to D_{5d}, but rather, to the rod group, $\mathcal{G}[5]$.[42,43] However, it has been shown[42–45] that the point group D_{10h} is isogonal to $\mathcal{G}[5]$. The character table[46] of the nondegenerate irreducible representations (irreps) of D_{10h} are shown in Table I and will be used to label the states of the SWNT that are invariant under cylindrical rotations by multiples of $2\pi/5$. The remaining degenerate irreps of D_{10h} correspond to Bloch states, which change phase under a $2\pi/5$ rotation, and can be ignored for the present purpose—as are the Bloch states associated with axial translations by multiples of z_0, that effectively span multiple unit cells.

For purposes of exploring all H atom dynamics of relevance for this paper, therefore—including migration of a chemisorbed H atom from a given carbon atom PES well to any of its neighboring wells—the effective unit cell size can be reduced by a factor of 5 by restricting the range of the cylindrical angle ϕ to $2\pi/5$. The resulting, "reduced unit cell" thus includes only four C atoms, as indicated in Fig. 3.

TABLE I. Subtable of the D_{10h} character table, showing all singly degenerate irreps used to label rovibrational states of the (5,5) SWNT-H system.

D_{10h}	E	$2C_{10}$	$2C_{10}^2$	$2C_{10}^3$	$2C_{10}^4$	C_{10}^5	$5C_2'$	$5C_2''$	i	$2S_{10}^4$	$2S_{10}^3$	$2S_{10}^2$	$2S_{10}$	σ_h	$5\sigma_d$	$5\sigma_v$
A_{1g}	1	1	1	1	1	1	1	1	1	1	1	1	1	1	1	1
B_{1g}	1	-1	1	-1	1	-1	1	-1	1	-1	1	-1	1	-1	1	-1
A_{2g}	1	1	1	1	1	1	-1	-1	1	1	1	1	1	1	-1	-1
B_{2g}	1	-1	1	-1	1	-1	-1	1	1	-1	1	-1	1	-1	-1	1
A_{1u}	1	1	1	1	1	1	1	1	-1	-1	-1	-1	-1	-1	-1	-1
B_{1u}	1	-1	1	-1	1	-1	1	-1	-1	1	-1	1	-1	1	-1	1
A_{2u}	1	1	1	1	1	1	-1	-1	-1	-1	-1	-1	-1	-1	1	1
B_{2u}	1	-1	1	-1	1	-1	-1	1	-1	1	-1	1	-1	1	1	-1

Note that the reduced unit cell is defined such that the center corresponds to the middle of a SWNT hexagon—what we term a "H-site" in Fig. 2. This is also taken to be the origin for the coordinates z and ϕ. Note that cylindrical coordinates (r, z, ϕ) are used throughout this paper to describe the position of the H atom. For the reduced unit cell, the coordinate ranges are thus $(-z_0/2 \leq z \leq z_0/2)$ and $(-2\pi/10 \leq \phi \leq 2\pi/10)$. The cylindrical locations of the four C atoms in the reduced unit cell are clearly evident in the figure.

Our initial goal is to construct a global 3D PES to describe the interactions of a single H atom with the (5,5) SWNT. The first step is to use DFT to compute explicit PES values for each of a number of *ab initio* grid points arranged in a regular cylindrical array. To this end we take full advantage of the D_{10h} symmetry of the SWNT in order to minimize the number of explicit DFT calculations required. We begin with a regular array of points in the (z, ϕ) subspace spanning the reduced unit cell. This array of cylindrical sites and their symmetry relationships are shown in Fig. 3. Note that the PES itself belongs to a singly degenerate irrep of D_{10h}, namely, the totally symmetric irrep A_{1g}. Consequently, explicit DFT calculations need only be performed over 1/8 of the reduced unit cell—a further reduction indicated by the
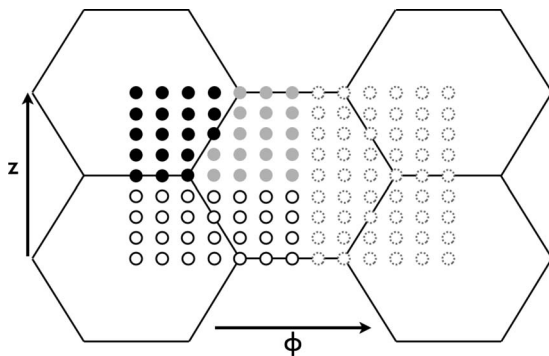

FIG. 3. Cylindrical sites within a single reduced unit cell, corresponding to z and ϕ coordinate values of grid points used for explicit DFT calculations (and PES fitting) for the (5,5) SWNT-H system. The solid black circles represent the sites explicitly computed using DFT. The solid gray circles are obtained from these via $\hat{i}_z$ inversion about one of four Z-sites (the one represented by the lowest solid black circle in the rightmost column of solid black circles). The black open circles are then obtained by applying $\hat{\sigma}_z$—a horizontal reflection about $z=0$—and the dashed open circles from a subsequent $\hat{\sigma}_\phi$ vertical reflection. The lower-rightmost gray filled circle is located at the origin of the reduced unit cell coordinates, $z=0$ and $\phi=0$—also known as an "H-site." The four corners of the reduced unit cell also correspond to H-sites, with the midpoints of the four rectangular boundaries corresponding to the E-sites.

solid black circles in Fig. 3. The solid gray circles are obtained by inverting the solid black circles about the Z-site (zigzag bridge). The open black circles are obtained by performing a mirror reflection in the z direction. Finally, the dashed open circles are obtained by performing a mirror reflection in the ϕ direction. Thus, of the full 9×13 reduced unit cell grid, only 18 cylindrical sites need be considered explicitly, for purposes of global PES construction. Orthogonal to this cylindrical array is a grid of radial points in r whose location and range are shown in Fig. 4.

The three symmetry operations, just described for duplicating the cylindrical sites across the entire reduced unit cell, commute with each other and combine together to give rise to the eight nondegenerate irreps of D_{10h}: A_{1g}, B_{1g}, A_{2g}, B_{2g}, A_{1u}, B_{1u}, A_{2u}, and B_{2u}. The three symmetry operations as described above correspond to the standard D_{10h} symmetry operations and irrep labels as follows:

$$\hat{i}_Z \cdot \hat{\sigma}_\phi \mapsto \hat{i} \qquad (g \text{ vs } u),$$

$$\hat{\sigma}_z \cdot \hat{\sigma}_\phi \mapsto \hat{C}_2' \qquad (1 \text{ vs } 2), \qquad (1)$$

$$\hat{i}_Z \cdot \hat{\sigma}_z \cdot \hat{\sigma}_\phi \mapsto \hat{C}_{10} \qquad (A \text{ vs } B),$$

where $\hat{i}_Z$ is inversion about the SWNT Z-site and $\hat{\sigma}_z$ and $\hat{\sigma}_\phi$ are reflections in the z and ϕ directions, respectively. The sign of the eight irreps under each of these three symmetry operations is indicated in the final column of Eq. (1) above, in Table I, and also in Fig. 5.

B. DFT calculations

Our first-principles electronic structure calculations make use of the fully self-consistent *ab initio* code SIESTA (Ref. 47) (Spanish Initiative for Electronic Simulations with Thousands of Atoms). The electronic energy is obtained from DFT[48,49] within the GGA (Ref. 50) as parametrized by Perdew, Burke, and Ernzerhof (PBE)[51,52] Nonlocal norm-conserving Troullier–Martins pseudopotentials[53] in the Kleinmann–Bylander form[54] are used to remove the core electrons from the calculation. The valence electrons are represented by pseudoatomic orbitals (PAOs)[55,56] using a split-valence double-ζ basis set with polarization functions (DZP). The basis set used for H is of the Sankey type[55] and has been shown to reproduce the properties of free H_2 very well.[57] It consists of two sets of $1s$ and one set of $2p$ PAOs. The basis set used for C is a new type[56] which is optimized (using a
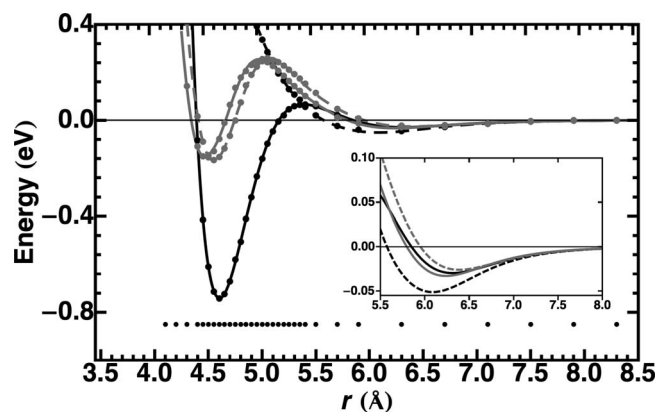
FIG. 4. PES slices along high-symmetry cylindrical sites, as a function of radial distance r, for the (5,5) SWNT-H system (subtract 3.45 Å from r to obtain distance from SWNT wall). The dashed black, solid black, dashed gray, and solid gray curves correspond to H-, A-, Z-, and E-sites, respectively, as obtained from the global analytically fit PES of this paper. The graph indicates a physisorptive region from about 5.75 to 7.5 Å, and a chemisorptive region between 4.45 and 5.0 Å or so (with a binding energy of around -0.75 eV). A barrier of $+54$ meV lies between the physi- and chemisorption wells. The circles along the bottom of the graph indicate the radial locations of the *ab initio* grid points, with corresponding DFT values also plotted as circles along the corresponding curves. The inset shows a closeup of the physisorption well, with local minimum along the H-site.

FIG. 5. Effect of SWNT symmetry operations on cylindrical coordinates, z and ϕ. The horizontal and vertical dashed lines represent the σ_z and σ_ϕ reflection planes, respectively. The filled black circles represent centers of inversion i_Z. The open circles are symmetrically equivalent sites on the SWNT, with + and − representing the relative sign values for a wave function belonging to the B_{1u} irrep.

downhill-simplex method[58]) for a C_{60} fullerene and made available by Romero via SIESTA's website.[59] C_{60} is the same diameter as our (5,5) SWNT which, therefore, has the same curvature in the equatorial direction. The optimized basis consists of two sets of $2s$, two sets of $2p$, and one set of $3d$ PAOs. The optimized geometry of the bare (5,5) SWNT (no hydrogen) is obtained first by performing conjugate gradient (CG) minimization[58] until the forces are less than 0.04 eV/Å. The resultant optimized (5,5) SWNT geometry is then used in all subsequent DFT calculations for the (5,5) SWNT-H system, which consist of only "single-point" calculations without further geometry optimization. Separate (5,5) SWNT-H calculations are performed for a large range of H geometries, however, as discussed in Sec. II A; all such calculations use spin polarization to deal with the odd electron on the hydrogen atom.

Three convergence parameters were adjusted to ensure the quality of the DFT calculations. The first two are tolerance parameters, which measure the allowed deviations from self-consistency for the computed electronic density and energy. The two tolerance parameters were varied over ten orders of magnitude, from 0.1 down to 1×10^{-10}. The computed energies became converged to within 0.1 meV, when the self-consistent density tolerance was set to 1×10^{-4} or less, and the self-consistent energy tolerance was set to 1×10^{-3} eV or less. Using these values, convergence was then determined with respect to the real space energy grid cutoff radius. A cutoff value of 200 Ry was found to result in final computed energies within 0.05 meV of a calculation with a cutoff of 700 Ry.

The DFT calculations are performed in a periodic supercell in Cartesian (x, y, z) space. To avoid self-interactions of the H atom with its periodic copies—and also to include the effe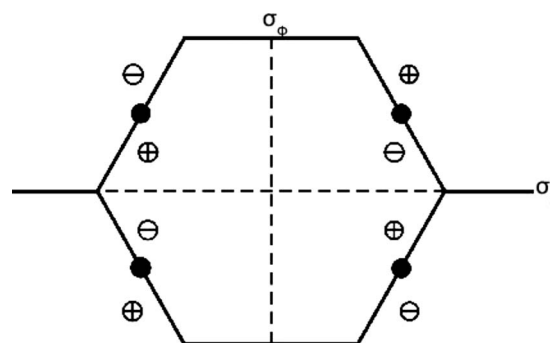ct of all relatively nearby C atoms—a sufficient number of SWNT unit cells must be included in the supercell, stacked one on top of the other in the z direction. Sufficient vacuum must also be added to the x and y (nonaxial) dimensions of the supercell (beyond the SWNT wall) to avoid periodic SWNT self-interactions in those directions and to ensure that long-range behavior of the SWNT-H system is adequately described. Initially, 5 Å of vacuum was added in both the x and y directions. Note that the unit cell height z_0 is not actually known prior to the bare SWNT geometry optimization calculation; the optimal value is obtained by simultaneously varying z_0 in step with the supercell height and minimizing the resultant energy for a single unit cell via the CG method. The resultant optimized single unit cell is then replicated three, four, and five times to form the initial guess for the supercell geometry containing 60, 80, or 100 carbon atoms, respectively, which are then themselves optimized in a second CG energy minimization step.

The SWNT-H interaction energy E(SWNT-H) was computed for each of the above supercells. We found that three SWNT unit cells are sufficient to ensure that H has virtually no interaction with its periodic image, greater in magnitude than ~ 0.05 meV or so. To test the long-range behavior of the SWNT-H interaction, the simulation cell was expanded by adding 10 Å of vacuum in the x direction (corresponding to the location of the H atom) beyond the SWNT wall, and E(SWNT-H) was then recomputed at several large radial values. By 5 Å from the SWNT wall, virtually no potential interaction remains (to ~ 0.05 meV or so). All subsequent DFT calculations as reported here therefore use the simulation supercell of three unit cells of SWNT, out to 5 Å beyond the SWNT wall in both x and y. The final supercell dimensions are thus $16.885 \times 16.885 \times 7.472$ Å^3. This corresponds to a SWNT unit cell height of $z_0 = 2.490$ Å.

Additional convergence testing of the Monkhorst–Pack[60] k-point sampling was also performed. A cubic grid of points is desired for sampling reciprocal momentum space (k-space). This is constructed by forming a special supercell with dimensions such that the reciprocal unit cell is cubic. The special supercell is formed by making a certain number of copies of the simulation cell in each direction—initially $i \times i \times \text{Round}[i/z]$, where i takes values of 1, 2, 3, etc., and is

the number of copies of the simulation supercell in the x and y directions. Since the final energy of the system depends on the k-point sampling, energy differences must be used to determine convergence. Therefore, for each value of i, energies are computed for both the bare optimized SWNT and a bare SWNT with a radius enlarged by 1% beyond the optimal value. The increase in energy, due to the expansion, was converged with respect to the value of i, with $i=3$ leading to results converged to within 0.5 meV. Thus, $3 \times 3 \times 7$, $3 \times 3 \times 5$, and $3 \times 3 \times 4$ are used for the three, four, and five unit cell calculations, respectively.

Unrelaxed, single-point (5,5) SWNT-H DFT calculations are achieved by setting the initial (5,5) SWNT geometry to the bare optimized value, and the number of CG steps to zero. The zero of energy is taken to be the desorption limit, i.e.,

$$E(\text{SWNT-H}) = E_c(\text{SWNT-H}) - E_c(\text{SWNT}) - E_c(\text{H}), \quad (2)$$

where $E_c(\text{SWNT-H})$, $E_c(\text{SWNT})$, and $E_c(\text{H})$ are actual energy values as computed by DFT for the SWNT-H, bare SWNT, and bare H atom systems, respectively. The global potential energy minimum is found to lie along the A-site (see Fig. 2) and corresponds to the chemisorption well. The minimum energy value for the three-unit-cell calculation differs from that of the four-unit-cell calculation by 7 meV and by 11 meV from that of the five-unit-cell calculation—i.e., by around 1% of the total chemisorption well depth. The average CPU times needed to compute the interaction energy at each geometry are 10, 40, and 70 h for the three-, four-, and five-unit-cell calculations, respectively. For the remainder of this paper, three-unit-cell calculations are used.

As per the deliberately detailed explication above, separate DFT calculations were performed for each of the SWNT-H *ab initio* geometries discussed in Sec. II A. The resultant radial desorption profiles for the four highest symmetry sites (Fig. 2) are indicated by the solid circles in Fig. 4. The distribution of radial points was chosen to be denser in radial regions that are more important (i.e., the chemisorption well), resulting in a nonuniform radial grid. The same radial grid was used for all DFT calculations reported in this paper—i.e., including those for the remaining 14 cylindrical sites of Fig. 3, not indicated in Fig. 4.

C. PES fitting

A global analytic fit to the *ab initio* points described above was obtained as follows. First a Fourier expansion in z and ϕ is performed, for which the expansion coefficients are taken to be r-dependent. The resultant PES is therefore of the form

$$V(r,z,\phi) = \sum_{i=0}^{4} \sum_{j=0}^{6} a_{ij}(r) \cos(iz') \cos(j\phi'), \quad (3)$$

where

$$z' = 2\pi(z/z_0)$$

and

$$\phi' = 5\phi.$$

In Eq. (3) above, the cylindrical coordinates are rescaled in order to emphasize the correct periodicity in both z and ϕ. The rescaled coordinates z' and ϕ' both range from $-\pi$ to π. Note also that the functional form of Eq. (3) behaves as the A_{1g} irrep under $\hat{\sigma}_z$ and $\hat{\sigma}_\phi$ reflections, as is appropriate for the potential energy function.

The summation limits in Eq. (3) come from the number of reduced unit cell grid points in the z and ϕ directions, after reductions due to σ_z and σ_ϕ reflection symmetries have been taken into account—i.e., 5 and 7, respectively, corresponding to the solid black and solid gray circles in Fig. 3. Consequently, for a given radial value r_k, the $a_{ij}(r_k)$ coefficients are uniquely determined via discrete Fourier transform. From the set of all $a_{ij}(r_k)$ for a given (i,j) cylindrical site, the curve $a_{ij}(r)$ is obtained by fitting to a functional form consisting of the sum of one Morse oscillator and two Gaussians, as follows:

$$a_{ij}(r) = \frac{\alpha_{ij}}{2} \exp[-\beta_{ij}(r - r_{ij})]\{2 - \exp[-\beta_{ij} \times (r - r_{ij})]\}$$
$$+ \alpha'_{ij} \exp\left[-\left(\frac{r - r'_{ij}}{\beta'_{ij}}\right)^2\right] + \alpha''_{ij} \exp\left[-\left(\frac{r - r''_{ij}}{\beta''_{ij}}\right)^2\right].$$
$$(4)$$

The Morse potential well is used to represent the primary chemisorption interaction. The two Gaussians then capture the (asymmetric) electrostatic barrier and physisorption well that are found at larger radial distances, as clearly seen in Fig. 4.

Finally, we point out that in Eq. (3), only terms for which $(i+j)$ is even are retained—or equivalently, $a_{ij}=0$ for $(i+j)$ odd. This is a symmetry restriction associated with the last symmetry operation, i.e., the $\hat{i}_Z$ inversion, and is the final condition needed to ensure that the resultant $V(r,z,\phi)$ PES correctly behaves as the totally symmetric irrep, A_{1g}. Table II lists the values of the parameters that define the $a_{ij}(r)$'s. These were obtained via a least-squares fitting, using the FINDFIT algorithm available in the program MATHEMATICA. The computed rms error for the fit of the global PES is 3.8 meV.

Figure 6 presents contour plots of cylindrical slices of the PES at three radial distances. See Sec. III A for a more specific discussion of PES features.

D. Quantum dynamics calculation

The full 3D nuclear motion Hamiltonian operator is given by

$$\hat{H} = \frac{\hat{p}_r^2}{2m} + \frac{\hat{p}_z^2}{2m} + \frac{\hat{p}_\phi^2}{2mr^2} + \hat{V}(r,z,\phi), \quad (5)$$

where m is the mass of the hydrogen atom, 1837.1527 a.u. In a typical DVR calculation,[40,41] a spectral variational basis representation (VBR) for each DOF is used to represent the corresponding position coordinate operator. Diagonalization of the resultant one-dimensional (1D) matrix representations then gives rise to the 1D DVR basis sets and grid points. In

TABLE II. Fitting parameter values for the radial functions $a_{ij}(r)$ used in the PES functional form as given by Eq. (4). Those values explicitly set equal to zero are denoted by the entry "0" (see footnotes).

	Morse			GAUSSIAN	1		GAUSSIAN	2	
ij	α_{ij} (eV)	β_{ij} (Å)$^{-1}$	r_{ij} (Å)	α'_{ij} (eV)	β'_{ij} (Å)	r'_{ij} (Å)	α''_{ij} (eV)	β''_{ij} (Å)	r''_{ij} (Å)
00	−1.044 191	1.913 27	4.745 84	0.284 503	0.441 23	4.789 55	0.435 472	0.751 35	4.975 40
02	0.057 545	2.914 43	4.802 86	−0.047 758	0.894 75	5.121 51	0.431 010	0.414 91	4.443 80
04	0.089 432	3.217 50	4.503 54	0^a	0^a	0^a	0.025 529	0.301 05	4.984 22
06	1.103 950	3.071 48	3.614 58	−0.011 265	0.258 93	5.072 72	−0.109 957	0.380 69	4.221 54
11	0.001 837	2.416 14	5.811 30	−0.113 004	2.089 32	2.524 87	1.982 576	0.617 00	4.147 95
13	−0.219 310	2.779 59	4.714 65	0^a	0^a	0^a	−0.201 793	0.357 32	4.737 47
15	0.013 309	3.770 18	4.632 48	0^a	0^a	0^a	−0.063 204	0.262 75	4.434 10
20	−0.000 015	4.530 15	5.324 93	−0.474 195	0.784 08	3.979 35	24.843 50	1.399 39	1.568 37
22	0.000 376	2.106 99	6.133 43	0.029 461	0.379 61	4.844 50	0.457 186	0.365 19	4.121 32
24	0.010 750	3.725 18	4.628 11	0^a	0^a	0^a	−0.060 148	0.316 08	4.456 33
26	−0.001 160	1.672 23	5.813 92	0^a	0^a	0^a	−0.090 589	0.373 27	4.184 45
31	0^b	0^b	0^b	−16.540 320	1.138 62	1.462 89	−0.008 497	0.084 42	4.517 26
33	−0.020 111	3.769 15	4.542 75	−5.006 266	−0.239 03	4.716 19	5.013 528	0.239 21	4.716 27
35	0^b	0^b	0^b	−1.220 846	0.328 15	4.173 30	1.207 877	0.335 04	4.167 65
40	−0.006 849	4.001 04	4.444 73	0.002 259	−0.058 79	4.562 25	0.001 821	0.229 69	4.742 29
42	0^b	0^b	0^b	−0.181 868	0.158 92	4.466 04	0.180 901	0.157 05	4.469 24
44	0.008 200	4.469 58	4.338 14	−1.412 409	0.157 43	4.445 63	1.411 044	0.156 71	4.446 26
46	−0.000 558	1.466 62	5.457 82	−0.009 669	0.162 08	4.275 53	−0.001 815	0.078 76	4.600 37

^{a}Set to 0 because fit placed r'_{ij} unphysically.
^{b}Set to 0 because fit was numerically 0.

this paper, we use a mixed approach, wherein we employ a DVR for the radial coordinate r and a Fourier basis in both the z and ϕ coordinates. This choice is convenient, given the Fourier representation of the PES in these coordinates [Eq. (3)], and also with respect to satisfying symmetry requirements perfectly for all nondegenerate D_{10h} irreps.

For the radial DVR, the PSO method[36–39] is used, for which a marginal Hamiltonian is constructed as follows:

$$\hat{H}^{\text{VBR}}_{\text{marg}} = \frac{\hat{p}_r^2}{2m} + \hat{V}_r(r). \quad (6)$$

In Eq. (6) above, $V_r(r) = \min V(r,z,\phi)|_{z,\phi}$ is the minimum of the potential energy at a fixed r value, with respect to z and ϕ. The VBR is then defined as the eigenstates of Eq. (6). To obtain these, the eigenproblem of Eq. (6) was itself solved using a radial sinc-DVR,[61] with 961 DVR points distributed uniformly between $r_{\text{min}} = 4.05$ Å and $r_{\text{max}} = 20.0$ Å. The lowest 20 eigensolutions were retained as the VBR basis for the 3D calculation. These 20 states are converged to at least 1×10^{-6} eV.

The orthonormal basis set used for the 3D calculation is therefore a direct product,

$$\Phi_{\alpha ij}(r,z',\phi') = \frac{1}{\pi}\left(\frac{1}{\sqrt{1+\delta_{i,0}}}\right)$$
$$\times \left(\frac{1}{\sqrt{1+\delta_{j,0}}}\right)\Delta_\alpha(r)\text{cs}(iz')\text{cs}(j\phi'). \quad (7)$$

In Eq. (7) above, $\Delta_\alpha(r)$ represents the radial PSO-DVR function centered around the DVR point $r = r_\alpha$ and "cs" represents either "sin" or "cos," i.e., the Fourier basis in z' and ϕ'. The maximum values of α, i, and j are thus the convergence

parameters for the 3D calculation. The D_{10h} irrep to which each of the Eq. (7) basis functions belongs is readily identified as follows. If $\text{cs}(iz') = \cos iz'/\sin iz'$, then the basis function is symmetric/antisymmetric under $\hat{\sigma}_z$. If $\text{cs}(j\phi') = \cos j\phi'/\sin j\phi'$, then the basis function is symmetric/antisymmetric under $\hat{\sigma}_\phi$. If $(i+j) = \text{even}/\text{odd}$, then the basis function is symmetric/antisymmetric under $\hat{i}_Z$. There are eight unique combinations of the above terms which correspond in one-to-one fashion with the eight nondegenerate irreps of D_{10h}, according to Table III.

The full 3D Hamiltonian matrix is given by

$$\mathbf{H}^{\text{DVR}}_{\alpha kl,\beta mn} = \mathbf{H}^{r,\text{DVR}}_{\alpha,\beta}\delta_{k,m}\delta_{l,n} - V_r(r_\alpha)\delta_{\alpha,\beta}\delta_{k,m}\delta_{l,n}$$
$$+ \mathbf{T}^z_{k,m}\delta_{\alpha,\beta}\delta_{l,n} + \mathbf{T}^\phi_{l,n,\alpha}\delta_{\alpha,\beta}\delta_{k,m} + \mathbf{V}_{\alpha kl,\beta mn}, \quad (8)$$

where $\mathbf{H}^{r,\text{DVR}}$ is the PSO-DVR matrix representation of Eq. (6), $\mathbf{T}^z_{k,m}$ and $\mathbf{T}^\phi_{l,n,\alpha}$ are the kinetic energies in the z and ϕ directions, respectively, and $\mathbf{V}$ is the potential matrix. Both kinetic energy matrices are diagonal in the Fourier basis employed here. For z, we obtain

$$\mathbf{T}^z_{k,m} = \left(\frac{2\pi}{z_0}\right)^2 \frac{k^2}{2m}\delta_{k,m}, \quad (9)$$

and for ϕ,

$$\mathbf{T}^\phi_{l,n,\alpha} = 25\frac{l^2}{2mr_\alpha^2}\delta_{l,n}. \quad (10)$$

We can write the potential matrix as
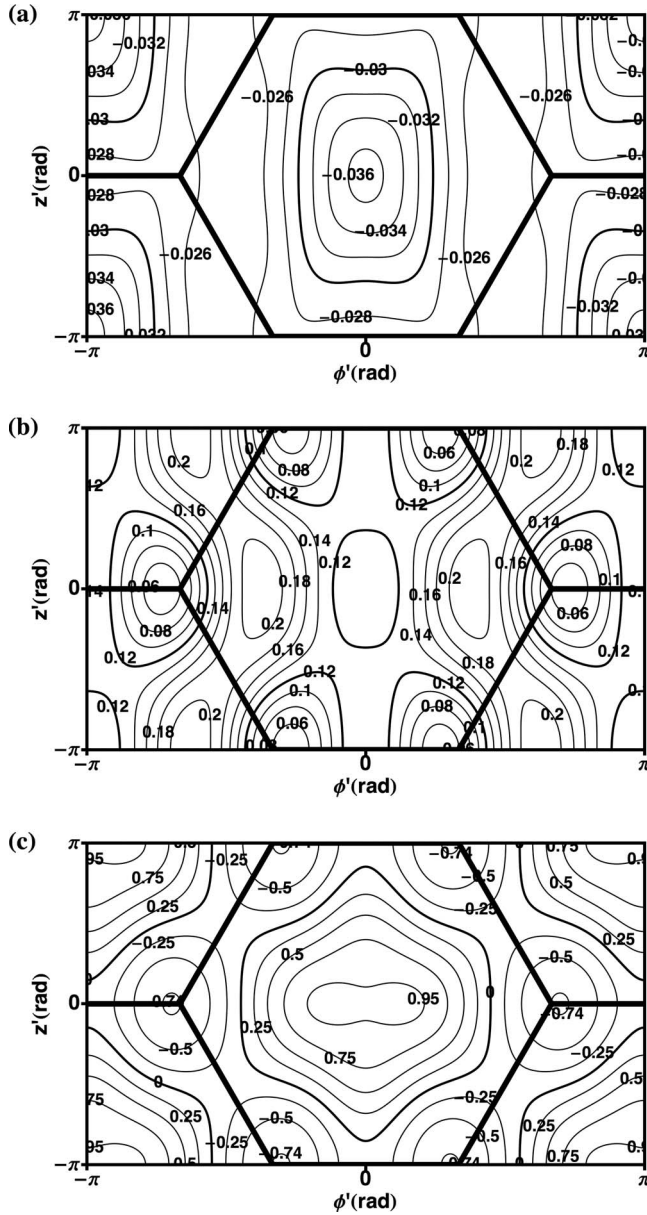
(a)

(b)

(c)

FIG. 6. Contour plots for the global analytic PES developed in this paper, as computed for three different "slices" along the cylindrical coordinates (z, ϕ) with fixed r values. (a) $r=6.5$ Å, the local minimum for the physisorption well, located at the H-site (center of plot). (b) $r=5.3$ Å, the chemi-physisorption isomerization transition state, located just off the A-site, in the direction of the E-site. (c) $r=4.6$ Å, the global minimum for the chemisorption well, located almost directly at the A-site. Thick black lines indicate the SWNT carbon-carbon bonds.

$$\mathbf{V}_{\alpha kl, \beta mn} = \sum_{i=0}^{4} \sum_{j=0}^{6} a_{ij}(r_\alpha) V_{mik}^{cs} V_{njl}^{cs} \delta_{\alpha,\beta}, \tag{11}$$

where $a_{ij}(r_\alpha)$ is the PES radial function of Eq. (4), evaluated at the αth grid point in r, and V^{cs} is comprised of Fourier representation matrix elements of $\cos(iz')$ or $\cos(j\phi')$. The explicit form of V^{cs} depends on whether the Fourier basis functions are sines or cosines. Note that for either z' or ϕ', D_{10h} symmetry forces both bra and ket basis functions to be of the same type, i.e., both sine or both cosine. If these are both cosine functions, then V^{cs} becomes

TABLE III. Correlations between cylindrical Fourier basis functions and the irreps of D_{10h}.

Basis function		D_{10h} irrep
$\cos(iz')\cos(j\phi')$	for $(i+j)$ even	A_{1g}
	for $(i+j)$ odd	B_{1u}
$\sin(iz')\cos(j\phi')$	for $(i+j)$ even	B_{2g}
	for $(i+j)$ odd	A_{2u}
$\sin(iz')\sin(j\phi')$	for $(i+j)$ even	A_{1u}
	for $(i+j)$ odd	B_{1g}
$\cos(iz')\sin(j\phi')$	for $(i+j)$ even	B_{2u}
	for $(i+j)$ odd	A_{2g}

$$V_{pqr}^{cos} = \frac{1}{\pi} \left(\frac{1}{\sqrt{1 + \delta_{p,0}}} \right)$$

$$\times \left(\frac{1}{\sqrt{1 + \delta_{r,0}}} \right) \int_{-\pi}^{\pi} \cos(p\theta)\cos(q\theta)\cos(r\theta)d\theta$$

$$= \begin{cases} \frac{1}{\sqrt{2}}\delta_{q,p} & \text{if } r=0 \text{ and } p>0 \\ \frac{1}{\sqrt{2}}\delta_{q,r} & \text{else if } p=0 \text{ and } r>0 \\ \frac{1}{2}\delta_{q,|p-r|} + \frac{1}{2}\delta_{q,p+r} & \text{else if } p \neq r \\ \frac{1}{2}\delta_{q,p+r} & \text{else if } p=r>0. \\ \delta_{q,0} & \text{else } p=r=0 \end{cases} \tag{12}$$

If bra and ket are both sine functions, then V^{cs} becomes

$$V_{pqr}^{sin} = \frac{1}{\pi} \int_{-\pi}^{\pi} \sin(p\theta)\cos(q\theta)\sin(r\theta)d\theta$$

$$= \begin{cases} \frac{1}{2}\delta_{q,|p-r|} - \frac{1}{2}\delta_{q,p+r} & \text{if } p \neq r \\ \delta_{q,0} - \frac{1}{2}\delta_{q,p+r} & \text{else } p=r>0. \end{cases} \tag{13}$$

In Eqs. (12) and (13) above, pqr represents mik for the z coordinate, or njl for the ϕ coordinate, and θ represents either z' or ϕ'. As stated previously, the maximum allowed values of i and j are 4 and 6, respectively. The corresponding maximum values for (k,m) and (l,n) must be at least this large and are taken as convergence parameters for the 3D calculation, as is the maximum value of α for the r coordinate. Note that the minimum index values are $p=r=0$ for V^{cos}, but $p=r=1$ for V^{sin}.

The identity of the first and second V^{cs} factors in Eq. (11)—as being either V^{cos} or V^{sin}—gives rise to four separate blocks of the potential matrix $\mathbf{V}$. These correspond naturally to the $\hat{\sigma}_z$ and $\hat{\sigma}_\phi$ reflection symmetries, and thus to a subdivision of the D_{10h} irreps, as per Eq. (1). To uniquely specify

TABLE IV. Computed rovibrational bound-state energies of the (5,5) SWNT-H system for all eight singly degenerate D_{10h} irreps. The number of digits listed corresponds to the convergence accuracy of the calculation, *or* to the number of digits needed to distinguish migration (i.e., tunneling) splittings, whichever is greater. All energies are given in eV, relative to the desorption threshold. Although the listed energies are all less than zero, the minus sign has been removed for visual clarity.

	A_{1g}	B_{1u}	B_{2u}	A_{2g}	B_{2g}	A_{2u}	A_{1u}	B_{1g}
1	0.496 624 39	0.496 624 36	0.496 624 35	0.496 624 38	0.371 928 93	0.371 930 17	0.371 930 16	0.371 928 92
2	0.384 150 3	0.384 149 5	0.384 149 3	0.384 150 1	0.262 930 8	0.262 961 1	0.262 961 0	0.262 930 6
3	0.276 463	0.276 452	0.276 444	0.276 455	0.159 825	0.160 229	0.160 223	0.159 819
4	0.255 082	0.255 076	0.255 075	0.255 081	0.139 778	0.139 783	0.139 782	0.139 777
5	0.247 530 2	0.247 516 7	0.247 516 6	0.247 530 1	0.128 374 73	0.128 515 84	0.128 515 84	0.128 374 73
6	0.173 65	0.173 54	0.173 45	0.173 56	0.061 94	0.065 51	0.065 47	0.061 89
7	0.147 90	0.147 57	0.147 56	0.147 89	0.035 6	0.037 2	0.037 1	0.035 5
8	0.140 92	0.140 79	0.140 78	0.140 91	0.027 024	0.028 337	0.028 336	0.027 023
9	0.077 2	0.076 5	0.075 4	0.076 2	0.010 48	0.010 55	0.004 022	0.002 87
10	0.053 6	0.048 7	0.048 6	0.053 4		0.000 23		
11	0.045 549	0.045 544	0.045 521	0.045 523				
12	0.036 5	0.036 2	0.036 0	0.036 3				
13	0.026 84	0.027 04	0.027 02	0.026 82				
14	0.024 54	0.024 49	0.016 14	0.017 259				
15	0.014 566 9	0.013 833 1	0.013 833 0	0.014 560 1				
16	0.013 86	0.010 962	0.004 200	0.009 09				
17	0.009 36	0.007 773	0.001 000	0.002 38				
18	0.003 85	0.003 55		0.000 85				
19	0.001 14	0.000 16						

individual D_{10h} irreps, however, we must further subdivide using $\hat{i}_Z$ symmetry, by distinguishing the odd $(k+l)$ [and $(m+n)$] case from the even case. Ultimately, this gives rise to eight distinct singly degenerate irrep blocks of the Hamiltonian matrix, which are then diagonalized independently to compute the corresponding eigenvalues and eigenvectors, using the EIGENSYSTEM algorithm within MATHEMATICA.

The maximum values of α, k, and l are the only convergence parameters for the quantum dynamics calculation described above. For all eight irrep combinations of the DVR basis of Eq. (7), convergence is reached using $\alpha_{max}=17$, $k_{max}=8$, and $l_{max}=20$. In order to determine convergence, we analyzed absolute differences between computed energies for calculations in which each convergence parameter was successively increased, keeping the other two constant. The calculation was considered to be converged when the maximum absolute energy difference for the lowest 50 rovibrational states (both bound and unbound), for each of the eight irreps, was less than 1 meV. The maximum absolute error for these 400 states is 0.87 meV, and the average absolute error is 0.12 meV. However, the vast majority of the bound states are converged to a much higher accuracy, as indicated in Table IV, which lists all of the computed bound-state energy levels for each of the eight irreps.

III. RESULTS AND DISCUSSION

A. PES

Figure 4 shows the radial potential energy profiles for the SWNT-H system, along the four high-symmetry sites of the SWNT (see Fig. 2). There are three different radial regions of interest that will be discussed in the following paragraphs.

For large r values, the PES is approximately flat in all directions. [see Fig. 6(a)]. However, there is some structure present. In particular, the PES predicts a physisorption well, with a local minimum lying above the H-site at $r=6.09$ Å, or 2.64 Å from the SWNT wall. The predicted well depth is 51 meV. The PES also predicts a transition state between neighboring physisorption wells, lying above the E-site at $r=6.23$ Å, with a barrier relative to the physisorption minimum of +17 meV. This is small, even compared to the well depth, suggesting that corrugation effects are minimal in the physisorption region—as has been previously observed, e.g., in graphite-H studies.[62–68] It should be stated though that the well depth as predicted here is not likely quantitative due to the inability of DFT to accurately describe long-range dispersion forces.

As the H atom approaches the SWNT from the physisorption well, it encounters an electrostatic potential barrier, separating the physisorption and chemisorption wells [see Fig. 6(b)]. In the process, the reaction path is steered away from the H-site channel and into the A-site channel, as the former becomes the potential maximum, and the latter the minimum (with respect to the z and ϕ coordinates), as the chemisorption well is approached. The corresponding transition state is a bit off the A-site, in the direction of the adjacent E-site, at $r=1.93$ Å from the SWNT [see Fig. 6(b)]. The barrier height for this physi- to chemisorption isomerization process is +54 meV, relative to the desorption threshold. Free H atoms at ambient T should therefore have no difficulty surmounting this barrier, to penetrate into the chemisorption region.

The chemisorption region lies completely within 1.5 Å or so of the SWNT wall—exhibiting a deep well with a (global) minimum energy of −755 meV, relative to the desorption threshold. The global minimum geometry is located
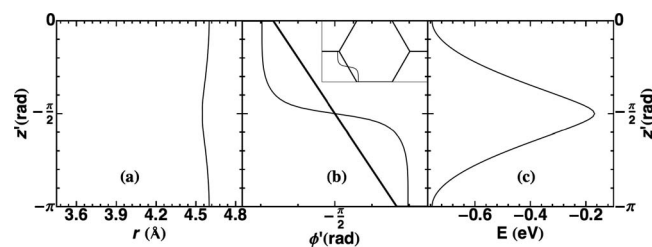
FIG. 7. Zigzag reaction pathway, connecting two adjacent (and equivalent) chemisorption minima, for the (5,5) SWNT-H system. Panel (a) shows how the radial coordinate r changes along the reaction path, as a function of the reaction coordinate z'. Panel (b) shows how the angular coordinate ϕ' changes along the reaction path, as a function of z'. The thick solid line across panel (b) shows the carbon-carbon bond. The inset of panel (b) is a zoomed-out view, in which the entire reduced unit cell is visible. Panel (c) is the reaction profile, showing energy as a function of z'.

very close to the A-site, at a distance of 1.15 Å from the SWNT. This is clearly shown in Fig. 6(c). There are two distinct reaction pathways connecting global minima in neighboring chemisorption wells. One of these lies directly along an equatorial C–C bond, with transition state at the E-site bridge. The second is a curvilinear path that roughly follows a zigzag bond, with a transition state at the Z-site. This pathway is shown in Fig. 7. The different reaction profiles for the two reaction paths are due entirely to curvature effects, i.e., for graphene, these pathways would be identical.

Although the reaction paths themselves are quite different, the Z-site and E-site transition states show similar characteristics; they are located respectively at 1.10 and 1.02 Å away from the SWNT wall, with respective barrier heights of 587 and 601 meV, relative to the chemisorption global minimum. (Note that these transition states correspond to the minimum of the E-site and Z-site radial potential curves in Fig. 4.) These results correctly suggest that corrugation effects play a very important role in chemisorptive dynamics, especially in the migration of H atoms from one C-atom well to another. Corrugation also exists in graphite-H studies, but is less pronounced, and often ignored in dynamical treatments.[62–68] On the other hand, one might also be tempted to conclude from these results that curvature plays only a small role, if any, in the migration dynamics, i.e., that migration is equally favorable along either pathway. As will be demonstrated in Sec. III C, such a conclusion would be premature.

A summary of the chief features of the PES is provided in Table V, which lists geometries and potential energies for the chemisorption and physisorption minima, as well as the four transition states that connect them.

B. Rovibrational bound states

The energy eigenstates as computed in Sec. II D correspond to the rovibrational bound states of the (5,5) SWNT-H system. From Table IV, the energy of the rovibrational ground state (i.e., the A_{1g} state in the upper left-hand corner) is seen to be $E_0 = -0.496\,625$ eV. This is about one-third of the way up the chemisorption well, implying a rather substantial ZPE of around 0.258 82 eV. Note that *all* bound rovibrational states are included in the table, including those with physisorptive and mixed chemi-physisorptive character.

TABLE V. Geometries and energies (relative to desorption threshold) for all stationary points (local minima and transition states) of the (5,5) SWNT-H system, as determined using the global analytical PES of Sec. II C. The "type" column distinguishes between minima and transition states, and also specifies where they occur (physisorption well, chemisorption well, or in between). The two distinct E-site and Z-site transition states that lie between adjacent chemisorption wells are referred to as "chemi-E-chemi" and "chemi-Z-chemi," respectively. All stationary points were found using the NMINIMIZE function within MATHEMATICA.

Type	r (Å)	z' (rad)	ϕ' (rad)	V (eV)
Minimum (physi)	6.093 76	0	0	−0.050 99
Minimum (chemi)	4.600 62	0	−2.187 20	−0.755 44
TS (physi-physi)	6.238 09	0	−π	−0.033 75
TS (chemi-physi)	5.382 49	0	−2.346 48	+0.053 74
TS (chemi-E-chemi)	4.467 32	0	−π	−0.153 83
TS (chemi-Z-chemi)	4.548 08	−π/2	−π/2	−0.167 51

There are a fair number of the latter, so that it is difficult to unambiguously specify the physisorption binding energy. However, the lowest-lying state with essentially pure physisorptive character appears to be the A_{1g} state on the left side of row 14 in Table IV. This state has an energy of −0.024 54 eV, about half way up the physisorption well. It should be borne in mind that the PES used here is not likely quantitatively accurate in the physisorption regime.

Regarding the eigenstate wave functions, formally, these are delocalized over the entire reduced unit cell—and by periodic extension, over the entire (5,5) SWNT. Even the low-energy eigenstates are "delocalized" in this sense, with equivalent pockets of probability density centered over each of the A-sites, as indicated in Fig. 8(a). However, since these pockets are almost completely isolated in their respective chemisorption wells, the delocalized low-energy eigenstates are essentially degenerate, and may therefore be linearly recombined into superposition eigenstates that *are* truly localized, i.e., one degenerate state per chemisorption well. The appropriate analogy here is the electronic structure of solid-state materials, in which context the above procedure may be readily understood. Indeed, the low-energy states described above correspond to core electrons, i.e., those that are tightly bound to individual atoms, and thus play little or no role in "conduction."

To understand conduction of electrons in solid-state materials, an analysis must be made of the valence electrons—or equivalently, single-electron states lying in the conduction-band characterized by significant electron density in the interstitial regions between the constituent atoms. A key idea of this paper is that a similar type of analysis will prove very useful in analyzing the *migration* of H atoms along SWNTs—or indeed, any other solid-state material. Such a picture has not been adopted previously, to the authors' best knowledge, but likely offers many advantages, e.g., in the many contexts where H atom/proton transfer is relevant. Perhaps the most compelling aspect of this approach is that much dynamical information can be gleaned from a detailed analysis of the *single*-particle (i.e., e^- or H atom) states, even for *many*-particle systems. At any rate, the
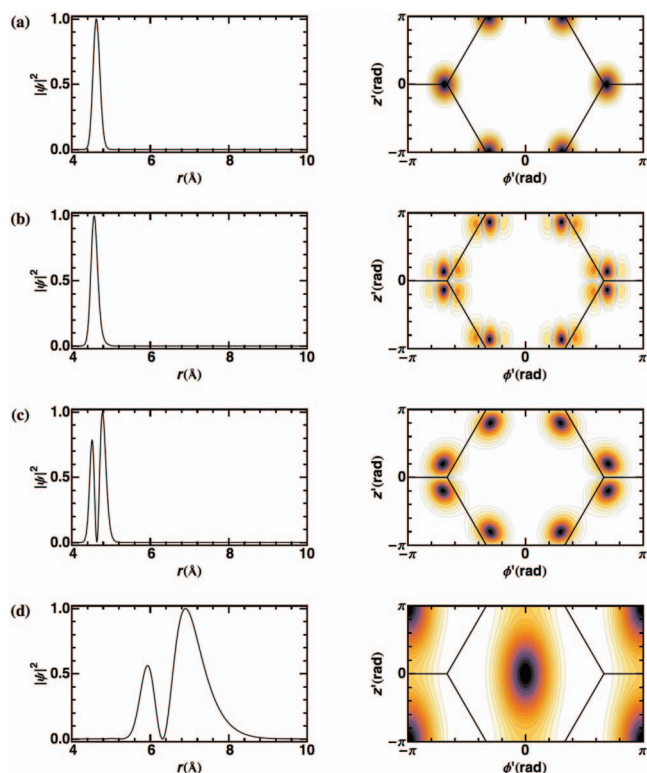
FIG. 8. (Color) Radial r probability densities (left) and cylindrical (z, ϕ) probability densities (right) for four bound rovibrational states of the (5,5) SWNT-H system. The former is obtained by integrating the eigenstate density $|\Psi(r,z,\phi)|^2$ over z and ϕ; the latter is obtained by integrating $|\Psi(r,z,\phi)|^2$ over r. Note that darker color correlates with higher density in these plots. (a) ground state, A_{1g}, $|000\rangle$, with energy of -0.4966 eV. (b) excited B_{2g} state, $|012\rangle$, with energy of -0.1594 eV, corresponding to a single excitation in z and a double excitation in ϕ. This state shows a large Z migration enhancement, despite higher excitation in ϕ than z. (c) excited A_{1u} state, $|110\rangle$, with energy of -0.1284 eV, corresponding to a single excitation in both r and z. This state shows the greatest Z migration enhancement. (d) highly excited A_{1g} state, with energy of $-0.003\,85$ eV, corresponding to a single excitation in r in the physisorption region; density is now centered around the H-site (center of right plot). A state label cannot be easily assigned to (d).

single-particle analysis is a logical starting point for more advanced treatments.

Returning to the (5,5) SWNT-H system, it is clear that H atom migration must be associated with the higher-lying rovibrational bound states for which significant probability

density may be found between C atoms—so that the chemisorption wells are no longer isolated [e.g., Fig. 8(c)]. Much like valence electron molecular orbitals or conduction-band states, these eigenstates are truly delocalized in space over many atoms. Whereas it is still possible to take linear combinations that give rise to localized wave functions in the sense described above, the latter are no longer eigenstates, and will therefore evolve over time. Indeed, this is the principal means we shall adopt for actually computing quantitative migration rates, as discussed in Sec. III C. This procedure is very much like using tunneling splittings for double-well systems to compute rates of migration from one well to the other (e.g., in NH_3)—except that in the (5,5) SWNT-H case, many wells are involved, and the highly quantum na-

ture of hydrogen implies that such "tunneling" splittings are discernible even at energies well above the transition state barriers.

To put the above into practice for H atom migration along the (5,5) SWNT, we must first establish the correct groupings and linear combinations of nearly degenerate irrep states. Formally, the construction of a *completely* localized state (i.e., centered around a single C atom only) requires consideration of all associated Bloch states across the entire (5,5) SWNT. The number of such states is proportional to the total number of C atoms, and therefore impracticably large for large systems. However, it is not necessary to work with completely localized states, in order to study H atom migration, or other dynamical effects. Partial localization—for which the superposition state densities are found over some C atoms but not others—will often suffice and can be achieved by restricting consideration to just a portion of the entire system.

In particular, restriction to just the reduced unit cell of the (5,5) SWNT (and associated singly degenerate D_{10h} irreps) enables sufficient localization for studying *both* of the two distinct migration pathways (i.e., through the E-site or the Z-site). The reduced unit cell includes four equivalent A-sites that can be thought of conceptually as the four corners of a square. The two horizontal edges of the square then correspond to equivalent E-site migration pathways, whereas the vertical edges symbolize the two Z-site pathways. In effect, the system is a "double double well," with two pairs of energy splittings per state. Localization over one of the four C atoms *within a reduced unit cell* is thus achieved via appropriate linear combination of eigenstates from a group of four irreps—although it must be borne in mind that this superposition state is in reality only *partially* localized, given that it has copies in each of the other reduced unit cells that comprise the total system.

The reduced unit cell A-sites/chemisorption wells that transform into each other under $\hat{\sigma}_\phi$ reflection are connected via the E-site migration pathway, whereas those that transform under $\hat{i}_Z$ are connected via the Z-site migration pathway. The remaining symmetry operation $\hat{\sigma}_z$, which is associated with the $\hat{\sigma}_h$ operation of D_{10h}, is not directly involved. Therefore, according to Eq. (1) and Table I, we expect eigenenergy splittings to occur in groups of four irreps, corresponding either to $(A_{1g}, A_{2g}, B_{1u}, B_{2u})$ or to $(B_{1g}, B_{2g}, A_{1u}, A_{2u})$.

These groupings are indeed borne out by the eigenenergy results as presented in Table IV, a list of computed energy values for all rovibrational bound states for the (5,5) SWNT-H system. Moreover, such assignments persist even above the E- and Z-site transition state barriers. For most of the entries in the table, the number of digits presented is equal to the convergence accuracy of the calculation. For the higher-lying energies, this is sufficient to discriminate tunneling—or more accurately, migration—splittings, which occur in two groups of two, as discussed above. However, for the low-lying "core electron" states, these splittings are extremely small, and so additional digits are presented as needed, in order to discern splittings. Note the right side of Table IV—corresponding to irreps that change sign under

$\hat{\sigma}_h$—exhibits roughly half as many rovibrational bound states as the left side. Presumably, this is because these left and right irrep groupings correlate, respectively, to doubly degenerate and singly degenerate irreps associated with the C_3 symmetry of graphene. For the left grouping, the degeneracy—but not the overall distribution—of energy levels is lifted by the presence of curvature in the SWNT.

The eigenvectors obtained from diagonalizing Eq. (8) provide the expansion coefficients for the basis functions of Eq. (7) and can thus be used to construct 3D wave functions and probability densities. Probability densities for several eigenstates are plotted in Fig. 8. Figure 8(a) shows the probability density in the radial r (left) and cylindrical (z, ϕ) (right) coordinates for the A_{1g} ground state. Note from the latter that the density is localized about all A-sites of the reduced unit cell, as per the above discussion. There is practically no probability density between C atoms, indicating that this eigenstate—together with the minimum energy eigenstates for the A_{2g}, B_{1u}, and B_{2u} irreps—corresponds via linear superposition to a localized core electron state. The higher-lying eigenstate of Fig. 8(b) shows a single excitation in z and a double excitation in ϕ, corresponding to the B_{2g} irrep. Despite the higher level of excitation in ϕ, enhanced probability density along the zigzag carbon-carbon bond is observed, relative to the equatorial bond. This trend characterizes the bound states throughout the energetic range, in fact, leading to important ramifications for the migration dynamics (Sec. III C). Figure 8(c) depicts the A_{1u} state with single excitations in both r and z, again with enhanced probability density along the zigzag bond. A correspondingly large Z-site migration rate is thus obtained (Table VII). From the left-hand plots, it is clear that all of the above states lie completely in the chemisorption region. At higher energies, however, physisorption can come into play. Figure 8(d) depicts a *pure physisorbed state*, with a double excitation in r. The (z, ϕ) density pattern is totally different than for the chemisorbed states. In particular, it is much more delocalized—reflecting the less important role of corrugation effects in the physisorption region—but also exhibits greatest probability density around the H-site, rather than the A-site, in keeping with the behavior of the PES.

C. Migration

As discussed in Sec. III A, detailed minimum energy paths and reaction profiles have been computed for both of the distinct migration pathways between adjacent chemisorption wells. These are referred to as the E and Z migration pathways, as they correspond to equatorial and zigzag carbon-carbon bonds, respectively. Although in the zigzag case, the correspondence is only a rough one, i.e., the actual reaction path wanders substantially off of the zigzag bond (Fig. 7), the two transition states lie exactly at the E-site and the Z-site, respectively. In both cases, the transition state radial value is slightly smaller than that of the chemisorption minimum near the A-site, as is evident in Figs. 4 and 7.

As discussed in Sec. III B, the bound rovibrational energy levels are grouped in sets of four that can be thought of as arising from a double double well. Two pairs of migration

TABLE VI. Irrep pairings associated with energy level splittings for each type of chemisorptive migration pathway, Z and E. The first irrep listed in each pair has +1 character under the defining symmetry operation for the corresponding migration pathway (i.e., $\hat{C}_2''$ for Z migration and $\hat{\sigma}_v$ for E migration), whereas the second has −1 character. The first two pairs for each migration pathway exhibit +1 character under $\hat{\sigma}_h$, and thus are grouped together; the second two pairs for each pathway exhibit −1 character under $\hat{\sigma}_h$, and are also grouped together.

Migration pathway	$\hat{\sigma}_h$ character	Irrep pairing
Z	+1	$A_{1g} \leftrightarrow B_{1u}$
	+1	$B_{2u} \leftrightarrow A_{2g}$
	−1	$B_{2g} \leftrightarrow A_{2u}$
	−1	$A_{1u} \leftrightarrow B_{1g}$
E	+1	$A_{1g} \leftrightarrow B_{2u}$
	+1	$B_{1u} \leftrightarrow A_{2g}$
	−1	$B_{2g} \leftrightarrow A_{1u}$
	−1	$A_{2u} \leftrightarrow B_{1g}$

pathways—one pair each for both Z and E types—are also seen to lie between the four A-site minima in the reduced unit cell and are expected to result in two different types of migration splittings, within the set of four energy eigenvalues. A precise determination of which splittings go with which migration pathway requires an association between migration pathways and symmetry operations, as was also already worked out unambiguously in Sec. III B. However, we find it helpful here to "translate" that discussion into the language of the D_{10h} symmetry group, as applied to the (5,5) SWNT.

It can be shown that the $\hat{C}_2''$ symmetry operation of D_{10h} corresponds to 180° rotation about the Z-site. This operation therefore directly corresponds to $\hat{i}_Z$ and Z migration, so that Z-splitting must be associated with irrep pairs that behave oppositely under $\hat{C}_2''$ (i.e., one irrep changes sign, the other does not). Similarly, $\hat{\sigma}_v$ is directly associated with $\hat{\sigma}_\phi$ and E migration, so that E-splitting irrep pairs behave oppositely under $\hat{\sigma}_v$. For both migration pathways, the character under $\hat{\sigma}_h = \hat{\sigma}_z$ must be the same for both irreps of the pair, as discussed earlier. Finally, the Z-migration irrep pair should have the same character under $\hat{\sigma}_\phi$, and the E-migration pair the same character under $\hat{C}_2''$, in order to yield partially localized states with respect to the respective migration types. The above rules give rise to unique irrep pair associations, for each type of migration, as indicated in Table VI. These can then be used to distinguish the two types of energy splittings, among the eigenenergy groups of four.

In effect, Table VI enables us to disentangle the two double wells in each grouping of four nearby energy eigenvalues. Each such grouping gives rise to *four* irrep pairs: two associated with E migration and two with Z migration. Each irrep pair then gives rise to an associated energy splitting,

$$E_\Delta = |E_+ - E_-|, \tag{14}$$

where E_+ is the energy of the eigenstate with +1 character under the defining symmetry operation for the corresponding migration pathway (i.e., $\hat{C}_2''$ for Z migration and $\hat{\sigma}_v$ for E migration) and E_- is the energy of the other eigenstate of the pair, which must have −1 character under the same opera-

TABLE VII. Computed migration rates for each energy grouping of four bound rovibrational eigenstates, in s⁻¹. Column 1: state assignments, *vis-a-vis* number of excitations in (r, z, ϕ). Column 2: average energy eigenvalue, in eV. Columns 3 and 4: the two k_E migration rates, with the first corresponding to the irrep pair with +1 character under $\hat{C}_2''$. Column 5: average of columns 3 and 4. Columns 6 and 7: the two k_Z migration rates, with the first corresponding to the irrep pair with +1 character under $\hat{\sigma}_v$. Column 8: average of columns 6 and 7.

$\lvert rz\phi\rangle$	E (eV)	k_E^1	k_E^2	$\bar{k}_E$	k_Z^1	k_Z^2	$\bar{k}_Z$
$\lvert 000\rangle$	−0.496 624 4	2.739×10^6	2.739×10^6	2.739×10^6	1.640×10^7	1.640×10^7	1.640×10^7
$\lvert 001\rangle$	−0.384 149 8	8.869×10^7	8.870×10^7	8.870×10^7	3.943×10^8	3.943×10^8	3.943×10^8
$\lvert 010\rangle$	−0.371 929 5	2.024×10^6	2.025×10^6	2.025×10^6	5.977×10^8	5.977×10^8	5.977×10^8
$\lvert 002\rangle$	−0.276 453 5	4.007×10^9	4.009×10^9	4.008×10^9	5.464×10^9	5.466×10^9	5.465×10^9
$\lvert 011\rangle$	−0.262 945 9	7.401×10^7	7.381×10^7	7.391×10^7	1.469×10^{10}	1.469×10^{10}	1.469×10^{10}
$\lvert 020\rangle$	−0.255 078 6	3.220×10^8	3.207×10^8	3.213×10^8	2.695×10^9	2.694×10^9	2.694×10^9
$\lvert 100\rangle$	−0.247 523 4	3.509×10^7	3.556×10^7	3.533×10^7	6.491×10^9	6.492×10^9	6.491×10^9
$\lvert 003\rangle$	−0.173 550 7	4.141×10^{10}	4.175×10^{10}	4.158×10^{10}	5.256×10^{10}	5.289×10^{10}	5.272×10^{10}
$\lvert 012\rangle$	−0.160 024 3	2.866×10^9	2.810×10^9	2.838×10^9	1.953×10^{11}	1.954×10^{11}	1.953×10^{11}
$\lvert 021\rangle$	−0.147 729 8	7.558×10^9	7.358×10^9	7.458×10^9	1.616×10^{11}	1.614×10^{11}	1.615×10^{11}
$\lvert 101\rangle$	−0.140 852 1	3.840×10^9	3.731×10^9	3.786×10^9	6.311×10^{10}	6.300×10^{10}	6.306×10^{10}
$\lvert 030\rangle$	−0.139 779 9	4.152×10^8	4.349×10^8	4.250×10^8	2.172×10^9	2.153×10^9	2.163×10^9
$\lvert 110\rangle$	−0.128 445 3	2.548×10^5	7.654×10^5	5.101×10^5	6.824×10^{10}	6.824×10^{10}	6.824×10^{10}
$\lvert 004\rangle$	−0.076 331 4	4.979×10^{11}	5.330×10^{11}	5.154×10^{11}	3.700×10^{11}	4.050×10^{11}	3.875×10^{11}
$\lvert 013\rangle$	−0.063 702 8	2.367×10^{10}	1.866×10^{10}	2.116×10^{10}	1.726×10^{12}	1.731×10^{12}	1.728×10^{12}
$\lvert 022\rangle$	−0.051 080 7	1.105×10^{11}	7.803×10^{10}	9.426×10^{10}	2.366×10^{12}	2.334×10^{12}	2.350×10^{12}
$\lvert 200\rangle$	−0.045 534 4	1.233×10^{10}	1.110×10^{10}	1.172×10^{10}	2.209×10^9	9.750×10^8	1.592×10^9
$\lvert 031\rangle$	−0.036 355 8	9.146×10^9	1.464×10^{10}	1.189×10^{10}	7.806×10^{11}	7.751×10^{11}	7.778×10^{11}
$\lvert 102\rangle$	−0.036 271 0	1.172×10^{11}	1.124×10^{11}	1.148×10^{11}	1.211×10^{11}	1.163×10^{11}	1.187×10^{11}

tion. A "migration rate" for the pair can then be computed in the standard manner used for tunneling rates for double-well systems, i.e.,

$$k = \frac{\pi\hbar}{E_\Delta}. \tag{15}$$

The migration rate quantity k is the inverse of the time required for a linear superposition state initially localized in one chemisorption well (or more technically, partially localized over one-half of the chemisorption wells) to refocus in a neighboring well (i.e., the remaining half of the chemisorption wells). Four separate migration rates can therefore be obtained from each energy level grouping; two for E migration and two for Z migration.

Table VII lists the migration rates, computed as described above, for each of the chemisorbed bound-state groupings, together with (group-averaged) energies, and normal mode assignments. The first migration rate listed of each type is for the pair that includes A_{1g} or B_{2g} (i.e., exhibits +1 character under both $\hat{C}_2''$ and $\hat{\sigma}_v$). The averaged migration rate for each type of migration pathway is also listed. The most significant trend is exactly what one might expect from a standard analysis of double-well tunneling, i.e., the migration rates increase roughly exponentially with increasing energy. This trend continues well above the transition state barriers—although above $E = -0.035$ eV or so, the assignments do become somewhat tenuous.

More interestingly, a completely unexpected trend was observed, pertaining to the *relative* magnitudes of k_E (equatorial migration rate) versus k_Z (zigzag migration rate), for the same grouping. In particular, a *substantial enhancement of k_Z* can be found throughout the energy range (except at the highest energies), with 15 of the 18 groupings showing

$k_Z > k_E$. Of course, higher ϕ excitations and lower z excitations tend to favor k_E relative to k_Z, but even some of these states show $k_Z > k_E$. On the whole, the k_Z enhancement is very pronounced, with four states, in particular—$\lvert 011\rangle$, $\lvert 012\rangle$, $\lvert 021\rangle$, and $\lvert 110\rangle$—presenting k_Z rates that are *two orders of magnitude* larger than the corresponding k_E rates. Only for the highest energies, just under the desorption threshold, does the enhancement appear to break down; however, these states are barely populated at ambient T.

The above fact, coupled with the fact that k_Z enhancement is observed throughout the relevant energy spectrum, is quite important for it implies that the enhancement should persist even under statistical Boltzmann averaging. We have performed such a statistical averaging over all bound rovibrational states at ambient temperature (i.e., at $T = 300$ K). The following Boltzmann-averaged thermal migration rates were obtained: $\bar{k}_Z(300 \text{ K}) = 3.03 \times 10^7$ s⁻¹; $\bar{k}_E(300 \text{ K}) = 4.86 \times 10^6$ s⁻¹. The corresponding statistically averaged Z-migration enhancement factor is greater than six times.

IV. CONCLUSIONS

The work presented in this paper is not likely to lead directly to a new hydrogen storage device, catalyst, or improved fuel cell; rather, our goal has been to shed new light on a mechanistic understanding of what actually happens dynamically when hydrogen interacts with materials, which may in turn prove to be of value to applied scientists and engineers working in the hydrogen fuel field. Achieving this aim requires not only that comprehensive quantum calculations be performed—for global PES construction, as well as subsequent dynamical calculation of the rovibrational eigenstates—but also new ways of framing the problem and

describing the results. We believe that this has been achieved in the present paper, at least to the extent possible for an initial foray such as this. At the very least, we hope to have demonstrated that quantum mechanics plays a vital role in properly understanding the dynamics of material substrate-hydrogen systems.

Among SWNT substrates, the (5,5) armchair SWNT considered here is small enough to exhibit substantial curvature, but large enough to be stable.[69] The global (5,5) SWNT-H PES of this paper is probably as accurate as can be achieved using DFT means, and is in any event carefully converged and thoroughly documented. It also rigorously satisfies proper A_{1g} symmetry restrictions. The spin-unrestricted aspect of the electronic structure calculations is obviously essential here, although this adds considerably to the total CPU cost. Interestingly, even without SWNT substrate relaxation (in a future study we will allow the SWNT to relax), the PES exhibits clearly demarcated chemisorption and physisorption well regions—unlike the corresponding graphite interaction,[62–68] for which no chemisorption is observed without substrate relaxation. This constitutes a rather striking "geometric" curvature effect, obviously due to the strained sp^2 structure of the SWNT, and suggests that the degree of puckering in the relaxed case is much more pronounced for graphite-H than for (5,5) SWNT-H. The unrelaxed PES of this paper may be applied, as is, to a range of dynamical processes involving both chemi- and physisorption (as implied by Table V), as well as desorption, etc. However, it should be stated that DFT may not predict physisorption to quantitative accuracy, as dispersion interactions are of necessity not included. Therefore, for future studies where physisorption and chemisorption are both important processes, we will use a switching function to smoothly transition between the H-SWNT PES and an improved long-range potential that more correctly captures the dispersion interactions, such as a semiempirical Lennard-Jones 6–12 PES, or perhaps even a PES computed at the MP2 level of theory.

In any event, the present PES is very well suited to the primary dynamical process considered in this paper, which is chemisorptive migration. Indeed, it might be argued that the unrelaxed PES of this paper is more appropriate in this context than a relaxed PES would be (although the latter will certainly be investigated in future), for two reasons. First, the high-lying states associated with the highest migration rates correspond to H-atom motion that may occur on a time scale (subpicosecond) faster than substrate relaxation. Second, regarding the single-particle rovibrational states computed here as the zeroth-order "molecular orbitals" for a multiparticle system in which there are many H atoms exohedrally chemisorbed, it is clear that the substrate geometry cannot simultaneously relax for all such adsorbates, but in the limit of complete coating, must adopt a cylindrical geometry as used here. Although the above use of electronic structure/solid-state terminology, applied in the context of hydrogen-material dynamical interactions, is to our knowledge new, we believe it is entirely appropriate and may generally prove to be very beneficial. At any rate, it offers a perspective and insight altogether different from that obtained using electronic structure alone and/or classical trajectory simulations.

In the new picture, after first computing the single-particle molecular orbital states as done here, more refined results can then be obtained by incorporating multiparticle correlation effects, symmetry restrictions, phonon excitations of the substrate, etc. This we certainly plan to do in future investigations.

On the other hand, for the present study of chemisorptive migration, only the single-particle states are needed. The term "migration" is used to distinguish this mechanism from diffusion, the process that is usually invoked to account for H-atom transport along SWNTs.[31,32,34,70] Diffusion requires numerous collisions among multiple adsorbates and a statistical, mixed-state (albeit possibly classical) description. In contrast, the migration mechanism proposed here is an entirely quantum dynamical effect that can be achieved with a single adsorbate within a pure-state formalism. In essence, it is simply a tunneling-splitting effect (in this case for a double double well), except that for hydrogen, it applies over a wide energetic range, both below *and above* the E- and Z-site saddle-point barriers. In principle, both migration and diffusion mechanisms may play a role in the axial motility of H atoms along the SWNT backbone. The migration rates for the lowest-energy states are not very high; however, migration rates increase by orders of magnitude as one moves up the energy spectrum, and for certain energies, may well prove competitive with diffusion.

In our quantum dynamical study of chemisorptive migration for the (5,5) SWNT-H system, we have treated both corrugation and curvature effects exactly. Regarding the latter, a curious situation is discovered, wherein the barrier to chemisorptive migration is essentially the same in all directions, yet the corresponding migration rates are greatly enhanced along the axial SWNT backbone (i.e., the "zigzag pathway"), in some cases by more than two orders of magnitude. From a hydrogen storage perspective, the above results may be significant in two ways. First, these results *could not* have been predicted without a proper quantum dynamical treatment. Indeed, as seen in Sec. III A, an analysis of the PES alone (even a detailed analysis) would incorrectly predict roughly equal migration rates along both pathways—or equivalently, that the curvature of the SWNT has little impact on the SWNT-H dynamics. This is now seen to be completely wrong, as the system does indeed display a pronounced *dynamical* curvature effect. In retrospect, this effect is likely due to different perpendicular ZPEs at the E-site and Z-site transition states, effectively lowering the barrier in the latter case.

The second significant conclusion is that the k_Z enhancement may help to explain the reversibility observed in spillover experiments. In general, reversibility is improved when there are a minimum of competing elementary reaction pathways or processes. At ambient T, desorption of chemisorbed H atoms is highly improbable (as is chemi- to physisorption isomerization)—thus greatly restricting radial motion. Moreover, a high k_Z enhancement substantially restricts azimuthal motion—effectively reducing the dynamics to 1D motion in z, along the SWNT backbone. This may prove very important when multiple H atoms are involved, *vis-a-vis* reducing the available competing pathways to the extent that revers-

ibility can be achieved. Together with the assumption of few desorbed particles (because all hydrogen is incident from the top in Fig. 1), this greatly restricts the available mechanistic pathways for a given adsorbed H atom and may help to explain why spillover as a whole is reversible.

To lend credence to the above, it would help to rule out energy transfer mechanisms that could lead to hydrogen desorption. Energy transfer from the SWNT substrate is likely to be minimal, owing to the mass mismatch and the relative stiffness of the substrate, as has been verified using quasi-classical trajectory calculations for both graphite-H_2 (Ref. 63) and SWNT-H_2 (Refs. 71 and 72) systems. The only other likely source of energy is thus a neighboring chemisorbed H atom, migrating in the same vertical channel. In practice, given the level of corrugation even along the zigzag path, the above adsorbate-adsorbate collision induced desorption (CID) process is less likely than say, a Langmuir–Hinshelwood recombination. Very preliminary potential energy calculations for (5,5) SWNT-H_2 indicate physisorption profiles with extremely steep/high PES values in the atomic chemisorption well region, however, thus suggesting that recombination is energetically highly unfavorable (the barrier appears to be at around +1.61 eV).[34] Note also that the reverse process is tantamount to spontaneous spillover without defects or metal atom decorations—a potentiality that is no longer seriously entertained in the literature.[73]

In any event, a definitive conclusion will require comprehensive two-particle quantum dynamics calculations to be performed. These will be the subject of future (5,5) SWNT-H_2 or (5,5) SWNT-H–H investigations, not only to elucidate the nature of neighboring chemisorbed H–H interactions along the zigzag channel but also to accommodate the case where there are free desorbed H atoms about. In particular, a dynamical calculation of the Eley–Rideal and desorbate-adsorbate CID processes will also be conducted, from which accurate desorption rates may be directly established. This is similar to previous investigations of graphite-H_2 scattering,[62–68] except that all six H-atom DOFs will be treated quantum mechanically. One anticipated feature of particular interest is the "secondary" binding enhancement, associated with two H atoms adsorbed on different but nearby A-sites. This effect can be quite pronounced and may well lead to a kind of "correlated" migration dynamics, which we plan to explore in the future. On the other hand, this effect may be less important when *every* A-site has an H atom attached—a situation we also plan to investigate.

Assuming that zigzag migration turns out to be the dominant mechanistic pathway for exohedrally chemisorbed H atoms, that it is the bottleneck of the spillover process, and that the one-particle picture developed here captures the core of the migration issue, one can start to ask questions about overall storage rates via the spillover mechanism, and to provide tentative, order-of-magnitude-type answers. Using the thermal migration rates computed at the end of Sec. III C for ambient T, and assuming one chemisorbed H atom per SWNT carbon atom, 3.5×10^8 H atoms may be adsorbed onto a single (5,5) SWNT each second. At this rate, it would take a fraction of 1 s to fully charge an array of 1 mm long SWNTs, which is certainly sufficiently fast for practical applications—although a great many other factors also come into play, of course. On the other hand, regardless of the effectiveness of the spillover catalyst, there is still a substantial ΔE (or ΔH) gap for the overall dissociative chemisorption process that must be overcome somehow. Including ZPEs, the dissociation energy for H_2 is $D_0 = 4.47$ eV, whereas the desorption energy for two chemisorbed H atoms on a (5,5) SWNT is close to 1.00 eV. To be sure, the latter number will increase substantially when two-particle calculations are performed, but a substantial ΔE is still likely to remain, one that is not easily accounted for by the kinetic energy of the incident H_2 molecules (at least not under thermal conditions).

In addition to the topics discussed above, various other subjects may merit future study, including zigzag and achiral SWNT substrates, endohedral binding, physisorption of molecular hydrogen (particularly as enhanced by the introduction of SWNT defects and metal atom decorations), etc.

ACKNOWLEDGMENTS

[1] U.S. Department of Energy Hydrogen Energy Website, http://www.hydrogen.energy.gov.

[2] A. C. Dillon, K. M. Jones, T. A. Bekkedahl, C. H. Kiang, D. S. Bethune, and M. J. Heben, Nature (London) **386**, 377 (1997).

[3] A. Chambers, C. Park, R. Baker, and N. Rodriquez, J. Phys. Chem. B **102**, 4253 (1998).

[4] P. Chen, X. Wu, J. Lin, and K. Tan, Science **285**, 91 (1999).

[5] C. Liu, Y. Y. Fan, M. Liu, H. T. Cong, H. M. Cheng, and M. S. Dresselhaus, Science **286**, 1127 (1999).

[6] L. Zhou, Y. Zhou, and Y. Sun, Int. J. Hydrogen Energy **29**, 319 (2004).

[7] M. Hirscher, M. Becher, M. Haluska, F. V. Zeppelin, X. Chen, U. Dettlaff-Weglikowska, and S. Roth, J. Alloys Compd. **356–357**, 433 (2003).

[8] A. C. Dillon, T. Gennet, J. L. Alleman, K. M. Jones, P. A. Parilla, and M. J. Heben, Proceedings of the 2000 Hydrogen Program Review (unpublished), Paper No. nREL/CP-507–28890.

[9] R. Yang, Carbon **38**, 623 (2000).

[10] S. Banerjee, S. Murad, and I. Puri, Proc. IEEE **94**, 1806 (2006).

[11] T. Lu, E. M. Goldfield, and S. K. Gray, J. Phys. Chem. B **110**, 1742 (2006).

[12] A. Ansón, M. A. Callejas, A. M. Benito, W. K. Maser, M. T. Izquierdo, B. Rubio, J. Jagiello, M. Thommes, J. B. Parra, and M. T. Martínez, Carbon **42**, 1243 (2004).

[13] S. Han and H. Lee, Carbon **42**, 2169 (2004).

[14] S. K. Bhatia and A. L. Myers, Langmuir **22**, 1688 (2006).

[15] R. Ruffieux, O. Gröning, P. Mauron, L. Schlapbach, and P. Gröning, Phys. Rev. B **66**, 245416 (2002).

[16] R. Ruffieux, O. Gröning, M. Bielmann, L. Schlapbach, and P. Gröning, Appl. Phys. A: Mater. Sci. Process. **78**, 975 (2004).

[17] A. Nikitin, H. Ogasawara, D. Mann, R. Denecke, Z. Zhang, H. Dai, K. Cho, and A. Nilsson, Phys. Rev. Lett. **95**, 225507 (2005).

[18] A. Nikitin, X. Li, Z. Zhang, H. Ogasawara, H. Dai, and A. Nilsson, Nano Lett. **8**, 162 (2008).

[19] S. Lee and Y. Lee, Appl. Phys. Lett. **76**, 2877 (2000).

[20] E. Lee, Y. Kim, Y. Jin, and K. Chang, Phys. Rev. B **66**, 073415 (2002).

[21] T. Yildirim, O. Gülseren, and S. Ciraci, Phys. Rev. B **64**, 075404 (2001).

[22] J. S. Arellano, L. M. Molina, A. Rubio, M. J. Lòpez, and J. A. Alonso, J. Chem. Phys. **117**, 2281 (2002).

[23] Y. Miura, H. Kasai, W. A. Diño, H. Nakanishi, and T. Sugimoto, Jpn. J.

Appl. Phys., Part 1 **42**, 4626 (2003).

[24] V. Barone, J. Heyd, and G. Scuseria, J. Chem. Phys. **120**, 7169 (2004).

[25] I. Cabria, M. Lòpez, and J. Alonso, Eur. Phys. J. D **34**, 279 (2005).

[26] S. H. Yang, W. H. Shin, J. W. Lee, S. Y. Kim, S. I. Woo, and J. K. Kang, J. Phys. Chem. B **110**, 13941 (2006).

[27] G. Gao, T. Cagin, and W. Goddard III, Phys. Rev. Lett. **80**, 5556 (1998).

[28] M. Shaijumon, N. Bejoy, and S. Ramaprabhu, Appl. Surf. Sci. **242**, 192 (2005).

[29] G. Che, B. Lakshmi, C. Martin, and E. Fisher, Langmuir **15**, 750 (1999).

[30] A. Lueking and R. Yang, J. Catal. **206**, 165 (2002).

[31] A. Lachawiec, Jr., G. Qi, and R. Yang, Langmuir **21**, 11418 (2005).

[32] R. Zacharia, K. Kim, A. Fazle Kibria, and K. Nahm, Chem. Phys. Lett. **412**, 369 (2005).

[33] F. Yang, A. Lachawiec, Jr., and R. Yang, J. Phys. Chem. B **110**, 6236 (2006).

[34] L. Chen, A. Cooper, G. Pez, and H. Cheng, J. Chem. Phys. **111**, 18995 (2007).

[35] A. Lueking and R. Yang, Appl. Catal., A **265**, 259 (2004).

[36] B. Poirier and J. C. Light, J. Chem. Phys. **111**, 4869 (1999).

[37] B. Poirier and J. C. Light, J. Chem. Phys. **114**, 6562 (2001).

[38] W. Bian and B. Poirier, J. Theor. Comput. Chem. **2**, 583 (2003).

[39] W. Bian and B. Poirier, J. Chem. Phys. **121**, 4467 (2004).

[40] S.-W. Huang and T. Carrington, Jr., J. Chem. Phys. **112**, 8765 (2000).

[41] R. G. Littlejohn, M. Cargo, T. Carrington, Jr., K. A. Mitchell, and B. Poirier, J. Chem. Phys. **116**, 8691 (2002).

[42] O. Alon, Phys. Rev. B **63**, 201403 (2001).

[43] O. Alon, J. Phys.: Condens. Matter **15**, S2489 (2003).

[44] M. Damnjanović, I. Milosević, T. Vuković, and R. Sredanović, Phys. Rev. B **60**, 2728 (1999).

[45] T. Vuković, I. Milosević, and M. Damnjanović, Phys. Rev. B **65**, 045418 (2002).

[46] T.-L. Li and J.-H. Ting, J. Vac. Sci. Technol. B **23**, 1682 (2005).

[47] J. M. Soler, E. Artacho, J. D. Gale, A. García, J. Junquera, P. Ordejón, and D. Sánchez-Portal, J. Phys.: Condens. Matter **14**, 2745 (2002).

[48] W. Kohn and L. Sham, Phys. Rev. **140**, A1133 (1965).

[49] N. Mermin, Phys. Rev. **137**, A1441 (1965).

[50] D. Langreth and M. Mehl, Phys. Rev. B **28**, 1809 (1983).

[51] J. Perdew, K. Burke, and M. Ernzerhof, Phys. Rev. Lett. **77**, 3865 (1996).

[52] J. Perdew, K. Burke, and M. Ernzerhof, Phys. Rev. Lett. **78**, 1396 (1997).

[53] N. Troullier and J. Martins, Phys. Rev. B **43**, 1993 (1991).

[54] L. Kleinman and D. Bylander, Phys. Rev. Lett. **48**, 1425 (1982).

[55] O. Sankey and D. Niklewski, Phys. Rev. B **40**, 3979 (1989).

[56] E. Anglada, J. Soler, J. Junquera, and E. Artacho, Phys. Rev. B **66**, 205101 (2002).

[57] J. M. Pruneda, S. K. Estreicher, J. Junquera, F. Ferrer, and P. Ordejón, Phys. Rev. B **65**, 075210 (2002).

[58] W. H. Press, B. P. Flannery, S. A. Teukolsky, and W. T. Vetterling, *Numerical Recipes*, 1st ed. (Cambridge University Press, Cambridge, 1989).

[59] Available from SIESTA's website, http://www.uam.es/siesta.

[60] H. Monkhorst and J. Pack, Phys. Rev. B **13**, 5188 (1976).

[61] D. T. Colbert and W. H. Miller, J. Chem. Phys. **96**, 1982 (1992).

[62] X. Sha and B. Jackson, Surf. Sci. **496**, 318 (2002).

[63] X. Sha, B. Jackson, and D. Lemoine, J. Chem. Phys. **116**, 7158 (2002).

[64] X. Sha and B. Jackson, J. Am. Chem. Soc. **126**, 13095 (2004).

[65] X. Sha, B. Jackson, D. Lemoine, and B. Lepetit, J. Chem. Phys. **122**, 014709 (2005).

[66] R. Martinazzo and G. F. Tantardini, J. Chem. Phys. **124**, 124702 (2006).

[67] R. Martinazzo and G. F. Tantardini, J. Chem. Phys. **124**, 124703 (2006).

[68] J. Kerwin, X. Sha, and B. Jackson, J. Phys. Chem. B **110**, 18811 (2006).

[69] C. Chen, X. G. Gong, and C. T. Chan, Phys. Rev. B **72**, 045444 (2005).

[70] X. Yang and J. Ni, Phys. Rev. B **74**, 195437 (2006).

[71] O. Stephan, P. M. Ajayan, C. Colliex, P. Redlich, J. M. Lambert, P. Bernier, and P. Lefin, Science **266**, 1683 (1994).

[72] Y. C. Ma, Y. Y. Xia, M. W. Zhao, M. Ying, X. Liu, and P. Liu, J. Chem. Phys. **115**, 8152 (2001).

[73] S. Dag, Y. Ozturk, S. Ciraci, and T. Yildirim, Phys. Rev. B **72**, 155404 (2005).